Journal of Porphyrins and Phthalocyanines
J. Porphyrins Phthalocyanines 2023; **27**: 797–810
DOI: 10.1142/S1088424623500499
Published at https://www.worldscinet.com/jpp/

Porphyrin metalla-assemblies coupled to cellulose nanocrystals for PDT and imaging applications

João C. S. Simões[a,c,d], **Georges Wagnières**[b], **Sophia Sarpaki**[c], **Vincent Sol**[d,◊], and **Bruno Therrien**[a,*]

[a]*University of Neuchâtel, Institute of Chemistry, Ave. de Bellevaux 51, CH-2000 Neuchâtel, Switzerland*
[b]*Laboratory for Functional and Metabolic Imaging, EPFL, CH-1015 Lausanne, Switzerland*
[c]*BioEmission Technology Solutions, 11472 Athens, Greece*
[d]*Université de Limoges, PEIRENE, EA 7500, 123 Avenue Albert Thomas, 87060 Limoges Cedex, France*

Received 16 November 2022
Accepted 30 January 2023

ABSTRACT: Photodynamic therapy (PDT) is an interesting and promising approach to tackle a broad spectrum of cancer. With the combination of a photosensitizer, light and oxygen, PDT achieves a unique selectivity by the production of localized reactive oxygen species (ROS) inside cells, which leads to their destruction. In addition, the luminescence properties of photosensitizers can be exploited to develop imaging tools. Unfortunately, the cancer selectivity and homogeneity of most photosensitizers are frequently limiting the performances of PDT and cancer detection/characterization by luminescence imaging. Consequently, our study aims to use cellulose nanocrystals to transport and deliver radiolabeled photo-responsive metalla-assemblies to create a new generation of theranostic agents for PDT and imaging applications. The synthesis, structural characterization, cytotoxicity evaluation, and *in vivo* biodistribution imaging of the compounds are presented. The best candidates show excellent biological activity and selectivity towards ovarian carcinoma cell line (A2780), cisplatin-resistant ovarian carcinoma cell line (A2780cis) versus normal human embryonic kidney cells (HEK293T), as well as efficient imaging properties, suggesting a potential use as multimodal theranostic agents.

KEYWORDS: photodynamic therapy, imaging, porphyrin, cellulose nanocrystal, metalla-assembly, theranostic agent.

INTRODUCTION

Cancer is estimated to be the second leading cause of death globally according to the World Health Organization, with a 9.6 million death count in 2018 [1]. To reduce the significant social, economic, psychological, and physical impact caused by cancer worldwide, efforts in early diagnosis, screening, treatment, and palliative care are needed.

An attractive cancer therapy that holds great promise for treating cancer is photodynamic therapy (PDT). This is mainly due to its precise controllability, minimally invasive nature, and high spatiotemporal accuracy [2]. However, even with these specificities, PDT still needs improvements, in particular concerning selectivity and targeting [3].

Nanocarriers stand at the forefront of nanomedicine research when it comes to drug targeting and delivery [4, 5]. Given that, solid tumors suffer from leaky vasculature and poor lymphatic drainage due to slacked junctions between endothelial cells, it is therefore possible to use this against them through a passive accumulation of nanoparticles (50–200 nm) [6, 7].

In order to take advantage of the enhanced permeability and retention (EPR) effect, nanoparticles must be able to stay intact in the bloodstream for a prolonged blood circulation time, with an ideal size of 100–200 nm [8,9], constituted of natural compounds and possessing a neutral and hydrophilic surface [10]. Among nanoparticles, those with PEG [11], with polysaccharide coating [12],

---

[◊] SPP full member in good standing.

*Correspondence to: Bruno Therrien, e-mail: bruno.therrien@unine.ch or cellulose nanocrystals (CNCs) emerge as of being of great interest. CNCs, in particular, are natural needle-like nanomaterials which possess several attractive characteristics such as renewability, low cost, and biodegradability [13]. They also present the great advantage of being non-toxic [14]. In addition, cellulose-derived materials have certain physico-chemical properties that provide them with synthetic advantages. For example, they can be easily functionalized, having a large number of hydroxyl groups present at the surface [15], and can range regarding their wide length distribution from 100 to 600 nm. Porphyrins have been previously attached to nanoparticles to modulate their antimicrobial, anticancer and catalytic properties as well as making them more water soluble [16–20]. Recently, Imlimthan *et al.* reported the use of modified CNCs as radiolabeled molecular imaging probes for *in vivo* medical applications [21]. However, most porphyrin derivatives are planar aromatic compounds that tend to aggregate in biological media, hampering their photophysical behavior [22]. A possible solution to limit aggregations between PS is their incorporation into supramolecular structures [23–25]. The benefit of using supramolecular metal-based assemblies to avoid aggregation has been recently reviewed by Sun and Stang [26]. We have in the past prepared porphyrin-based metalla-assemblies to avoid aggregation and to increase water solubility of PS [27]. For example, a series of arene ruthenium metalla-cubes built from tetrapyridylporphyrin panels (Fig. 1) have showed excellent PDT activity on cancer cells [28–30], as well as on fibroblast-like synoviocytes [31].

These octacationic complexes are water soluble and show no aggregation in biological media, probably due to steric and electrostatic repulsion. Moreover, as also previously demonstrated by different authors, they possess an excellent photoactivity, with a tremendous phototoxicity index [32, 33], thus showing great potential as a new generation of PDT agents.

It is also widely recognized that accurate cancer detection is imperative towards successful treatments. Only by identifying the area the tumor is situated at, recognizing the kind of cancer, its limits and whether the disease is restricted or has metastasized to different organs, it is possible to truly give the best treatment for the patient and consequently obtain the most ideal result. It is therefore obvious that when choosing a specific cancer treatment methodology, diagnostic agents assume a critical role [34, 35]. Knowing this, imaging is crucial in the treatment, and interestingly, photosensitizers can be used not only to treat (PDT), but also to visualized cancer [2]. An elegant strategy to add imaging properties to photosensitizers is by the attachment of radioactive isotopes. Indeed, insertion of a radionuclide at the core of a porphyrin-based PS is relatively easy to achieve and has showed great potential for imaging [2, 36–38], the most common isotopes used in this manner being copper-64 [39], gallium-68 [40], technetium-99m [41], and indium-111 [42].

Herein, we present an extension to our versatile system, adding two more functionalities to the arene ruthenium porphyrin-based metalla-assemblies. The insertion of technetium-99m in the core of the pyridylporphyrin panels aims to incorporate imaging properties, while the covalent grafting of the arene ruthenium metalla-assemblies to cellulose nanocrystals targets the EPR effect. The influence on the PDT efficiency upon introduction of these new characteristics has been evaluated on cancerous (A2780 and A2780cis) and non-cancerous (HEK293T) cell lines, showing that both additions have a positive impact on the *in vitro* activity. In addition, preliminary *in vivo* imaging experiments show the biodistribution of the compounds, confirming their imaging properties.

RESULTS AND DISCUSSION

Supramolecular arene ruthenium metalla-assemblies are built from two main components, dinuclear arene ruthenium metalla-clips, and multidentate N-donor connectors (panels) [43]. These components can be functionalized to modify the physico-chemical properties of metalla-assemblies [2, 44]. Therefore, to introduce imaging and grafting opportunities, functionalized tris-pyridyl-porphyrin panels were used (Fig. 2). In these panels, the replacement of a pyridyl group by an hydroxyphenyl or aminophenyl group provides a fixation point for the insertion of cellulose nanocrystals, while keeping two photosensitizers within the supramolecular structure. The porphyrin derivatives (5-(4-hydroxyphenyl)-10,15,20-tris(4-pyridyl)porphyrin) (**P1**) and (5-(4-aminophenyl)-

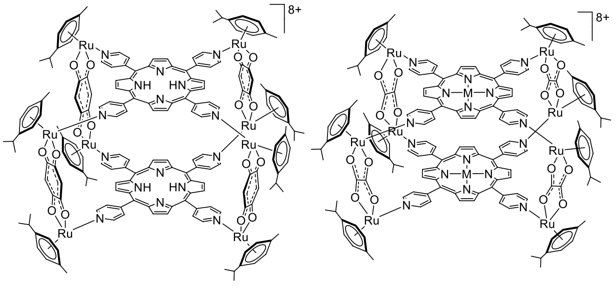

Fig. 1. Two porphyrin-based arene ruthenium metalla-cubes previously used as PDT agents [25].

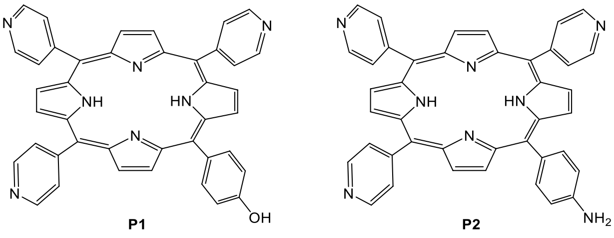

Fig. 2. Molecular structures of the functionalized tris-pyridyl porphyrin derivatives **P1** and **P2**.

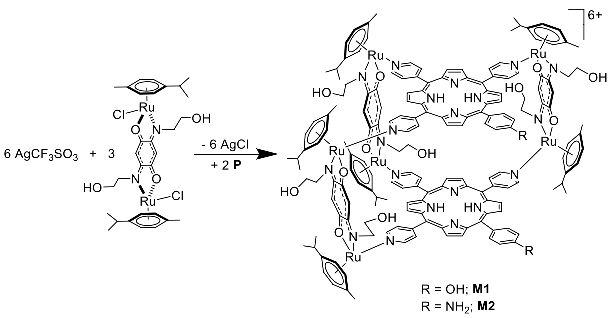

Scheme 1. Synthesis of metalla-assemblies **M1** and **M2**.

10,15,20-tris(4-pyridyl)porphyrin) (**P2**) were prepared according to the literature [44, 45].

From the tris-pyridyl porphyrin derivatives **P1** and **P2**, the synthesis of the metalla-assemblies is straightforward. As illustrated in Scheme 1, the first step is to react the dinuclear arene ruthenium metalla-clip [$Ru_2(\eta^6$-*p*-cymene$)_2${2,5-bis(2-hydroxyethylamino)-1,4-benzoquinone}Cl_2] with silver triflate, followed by the addition of the corresponding panel, respectively **P1** and **P2**. Then, the hexacationic metalla-assemblies **M1** and **M2** are isolated in good yield as their triflate salts (see Exp. part). The molecular structure of these two metalla-assemblies was confirmed by a combination of NMR spectroscopy and mass spectrometry.

Upon the formation of the metalla-assemblies **M1** and **M2**, the ^{1}H NMR signals (Figs. S1 and S2, supplementary information) assigned to the metalla-clip can still be observed, while new signals associated with the porphyrin panels appear (10.0–7.5 ppm, aromatic signals of H-β pyrrolic proton and *meso* aryl groups). These observations are consistent with the formation of the metalla-assemblies.

The *p*-cymene moieties show peaks around δ ~1.3–2.5 ppm for the protons of the isopropyl and methyl groups (alkyl protons), and signals in the 6.0–5.3 ppm region corresponding to aromatic protons. Around 9.1–8.0 ppm, more aromatic signals can be found corresponding to the pyridyl and β-pyrrolic protons of the porphyrin moieties. In addition, at ~3.8–3.5 ppm, the benzoquinone aryl protons are observed. In complexes **M1** and **M2**, additional signals at ~ 4.73 and 5.98 ppm can be found for the protons of the hydroxyl and primary amine protons of the hydroxyphenyl and aminophenyl substituents at the *meso* positions of both porphyrins, while peaks of the porphyrinic NH protons were observed at -2.9 ppm. Finally, at δ ~ 4.1 ppm, a peak corresponding to the benzoquinone hydroxyl protons is observed.

Mass spectrometry (Figs. S3 and S4, supplementary information) provides further evidence for the formation of the metalla-assemblies. A series of peaks with different charge states from 3+ to 6+ were observed for both **M1** and **M2**, because of the loss of the triflate (OTf−) counterions.

UV-Vis absorption and fluorescence spectra were measured in DMSO for both porphyrins (**P1** and **P2**) as well as their corresponding metalla-assemblies **M1** and **M2**. Their absorption spectra were determined using a 1 mM concentration (Figs. S5 and S6, supplementary information) showing the typical Soret band (413 and 417 for **P1** and **P2**; 412 and 415 nm for **M1** and **M2**, respectively) and Q-bands (region of 450–600 nm) of porphyrin-based compounds, which are attributed to the absorption transition between the ground state and the first excited singlet state (S0−S1).

Then, the two metalla-assemblies were combined with cellulose nanocrystals (CNCs). Prior to the grafting, CNCs were obtained by hydrolysis of cellulose with a sulfuric acid solution (64% w/w) followed by several washings, centrifugation, and dialysis against distilled water until neutrality [17]. The purpose of this acid hydrolysis consists of breaking cellulose chains within the amorphous domain, thus getting free nanocrystals, which can then be selectively oxidized in primary alcohols with TEMPO. The obtained CNCs suspension can be easily linked to other moieties through the newly added carboxylic acid groups, thus forming with **M1** and **M2**, the corresponding metalla-assembly grafted to CNCs, **MC1** and **MC2** respectively (Fig. 3).

The FTIR spectra of CNCs precursor, **MC1** and **MC2** (Fig. S8) in the wavenumber range of 3700 - 2900 cm^{-1}, showed similar bands of cellulose around 3360 cm^{-1} (O-H stretching), 2890 cm^{-1} (C-H stretching), 1430 cm^{-1} (CH_2 symmetrical bending), and 1057 cm^{-1} (ether C-O-C) [44]. The spectrum of oxidized CNCs also displayed a signal at 1720 cm^{-1} due to the carbonyl stretching of the carboxylic acid function [16]. Compared to the CNCs precursor, the FTIR spectra of **MC1** show a strong peak at 1739 cm^{-1}, which suggests the presence of an ester bond, presumably between the hydroxyl group of the porphyrin in metalla-assembly **M1** or the hydroxyl groups in the alkyl chain of the metalla-assembly with the cellulose nanocrystals [46]. On the other hand, a peak around 1644 cm^{-1} for **MC2** suggests the presence of an amide bond between the carboxylic function of CNCs and the amine group of porphyrin [44]. Simultaneously, the ATR FT-IR spectrum of both CNCs-linked metalla-cages

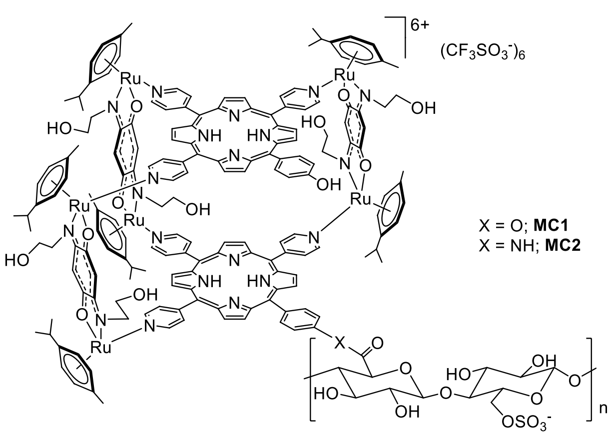

Fig. 3. Molecular structures of **MC1** and **MC2**.

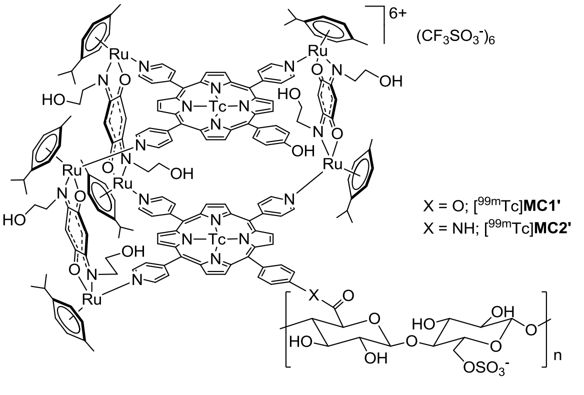

Fig. 4. Proposed molecular structures of [^{99m}Tc]**MC1′** and [^{99m}Tc]**MC2′**.

showed that the intensities of the C–H vibration band of methyl groups (2820–2976 cm^{-1}) are strengthened. The N–H bending vibration peak of porphyrin units appeared at 1658 cm^{-1}. All these indicate the successful combination of CNCs with the metalla-assemblies. The UV-Vis of **MC1** and **MC2** (Fig. S7) also show a hypsochromic shift of the Soret and Q-bands, with the Soret band appearing at 425 and 427 nm, respectively, further suggesting the grafting of **M1** and **M2** to CNCs.

Radiochemistry

After the syntheses and characterizations, radiolabeling experiments were performed to determine if these supramolecular assemblies can be used as multimodal imaging agents.

First, we have determined the importance of reaction time, stoichiometry, and temperature in the formation of the radiolabeled products. Moreover, for comparison, the incorporation of technetium-99m in **P1** and **M1** was also performed. Interestingly, time and temperature have a significant impact on the nature of the compound, and the best conditions for the radiolabeling of these compounds were at 60°C for a minimum of 45 minutes; any temperature or reaction time inferior to these gave a poor radiolabeling completion and/or a mixture of compounds. After having established these conditions, labeling with technetium-99m was performed (Fig. 4), with the incorporation of over 90% for both [^{99m}Tc]**MC1′** and [^{99m}Tc]**MC2′** CNCs grafted metalla-assemblies.

Under the same conditions, the radiolabeling of **P1** and **M1** was achieved, resulting in the incorporation of technetium-99m in the core of the porphyrin of 93 and 98%, respectively, which are similar to those found for the CNCs-grafted compounds.

The stability of the [^{99m}Tc]-derivatives were also evaluated. Figure 5 shows the successful radiolabeling of these compounds, and the stability at 37°C of [^{99m}Tc]**MC1′** in different media at different time points, to better replicate physiological conditions, from 15 minutes to up to 24 h. The different media for the radiochemical purity studies were chosen with the intent of mimicking the main components of the bloodstream. In addition, since EDTA and DTPA form stable complexes with most transition metals such as Cu, Tc, and Zn, the behavior of these compounds in DTPA and EDTA solutions were also studied.

Finally, it was also important to verify the stability of these compounds in HEPES and NH_4AcO buffer solutions, because they are the main buffers used for radiolabeling studies. From these experiments, it was possible to determine that there is no significant difference for at least 24 h when it comes to the radiochemical purity under most of the media tested, with some differences occurring mainly in the cases of EDTA and plasma, right after 15 min. However, after this time point, they seem to stay stable for the rest of the study. This could be due

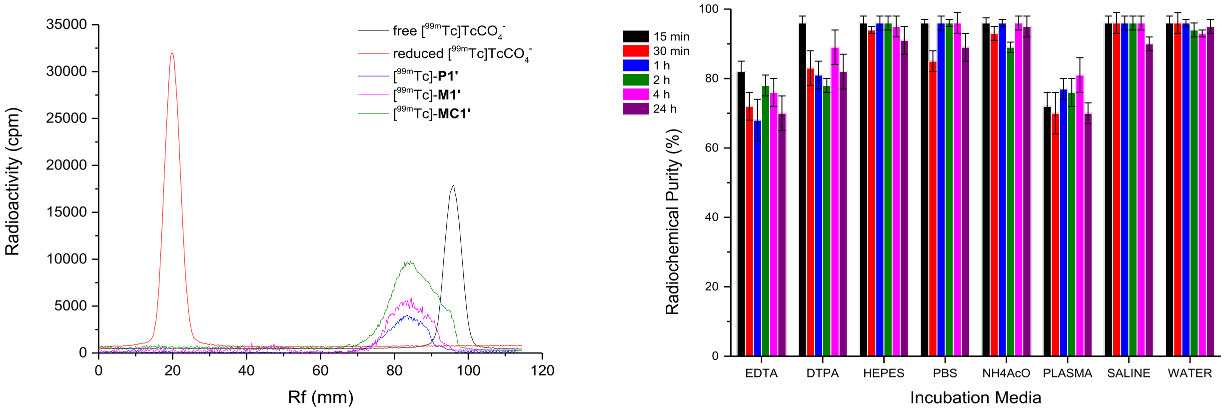

Fig. 5. Radio-TLC chromatographic data of “free” and reduced [^{99m}Tc]pertechnetate ([^{99m}Tc]TcO_4^-]), and ^{99m}Tc-radiolabeled compounds, with “cpm” standing for counts per minute, which is a measure of radioactivity, more specifically the number of atoms in a given quantity of radioactive material that are detected to have decayed in one minute. The radio-TLCs were developed on Whatman 1 MM with saline as the mobile phase showing, ROI ≥ 90.0%. (right); and Graph presenting the results obtained from radiochemical purity tests of [^{99m}Tc]**MC1′**(left). The radioactive molecule was incubated at 37°C with different media (1:10) for up to 24 hrs. Error bar stands for standard error (±SE), calculated from three repeated measurements.

Table 1. IC_{50} values ± standard deviation (in μM) of both porphyrins, corresponding metalla-assemblies, and metalla-assemblies linked to the CNCs against two ovarian carcinoma cell lines (A2780 and A2780cis) and one hepatic healthy cell line (HEK293T).

	Cell lines					
	A2780cis		A2780		HEK293T	
	Without irradiation	Irradiated	Without irradiation	Irradiated	Without irradiation	Irradiated
P1	61.01 ± 2.67	1.41 ± 0.08	52.30 ± 4.50	1.30 ± 0.09	43.61 ± 4.01	3.57 ± 0.42
M1	6.79 ± 0.70	0.33 ± 0.05	4.52 ± 0.28	0.10 ± 0.02	27.1 ± 1.50	0.50 ± 0.11
MC1	0.96 ± 0.03	0.12 ± 0.01	1.65 ± 0.27	0.10 ± 0.01	1.88 ± 0.72	0.19 ± 0.01
P2	32.03 ± 2.41	0.41 ± 0.01	28.81 ± 3.92	0.40 ± 0.04	25.14 ± 1.73	0.41 ± 0.01
M2	7.11 ± 0.58	0.61 ± 0.09	2.43 ± 0.21	0.90 ± 0.03	4.35 ± 0.32	1.84 ± 0.13
MC2	0.89 ± 0.02	0.17 ± 0.02	0.82 ± 0.03	0.12 ± 0.01	0.86 ± 0.44	0.24 ± 0.01
Cisplatin®	26.01 ± 3.01	-	2.02 ± 0.92	-	48.02 ± 3.36	-
RAPTA-C	>200	-	>200	-	>200	-

to the fact that EDTA is a strong chelator of technetium-99m, and that plasma also has components such as magnesium ions that can compete with technetium for the coordination with the center of the porphyrin units. In any case, it should be noted that cellulose-based materials have been used as absorbents for ^{99}Tc in the past [53], thus, simple absorption on CNCs cannot be ruled out.

In vitro studies

Following the stability study, the cytotoxicity of the metalla-assemblies, along with their corresponding porphyrins and cellulose grafted compounds (Scheme 1, Figs. 2 and 3), were evaluated on two different human ovarian carcinoma cancer cell lines, A2780 and A2780cis, as well as on the human liver cell line HEK293T. The results (Table 1) of their metabolic activity inhibition against all cell lines (IC_{50}) are presented in the form of dose-response curves in Figs. 6 and 7.

Regarding **P1** and its corresponding metalla-assembly **M1**, although the porphyrin by itself showed IC_{50} values after irradiation between 1 μM and 3 μM (Table 1, first line), when it is further functionalized (Table 1, second line) it shows higher cytotoxicity with IC_{50} values up to only 0.5 μM. It must be noted that the IC_{50} values in the dark for all the compounds were at least 10x lower than those after irradiation. When it comes to **P2** (Table 1, fourth line), and its corresponding metalla-assembly **M2** (Table 1, fifth line), the same results can be observed with lower IC_{50} values under both conditions.

In the dark, the metalla-assemblies (**M1** and **M2**) are more cytotoxic than the porphyrins (**P1** and **P2**). Upon irradiation, however, an interesting result is observed: **P2** appears to be a better PDT agent than the corresponding metalla-assembly **M2** (Table 1, fourth and fifth lines). In addition, we can notice better IC_{50} values for the aminophenyl porphyrin when compared to its hydroxyphenyl analogue (Table 1, first and fourth lines), but higher IC_{50} values when both metalla-assemblies are being compared, **M1** and **M2** respectively (Table 1, second and fifth lines). This suggests that the difference in activity of the two porphyrins can be most likely linked to their phenol and amino groups and that when we further functionalized these porphyrins by conjugation with metalla-clips, it seems that for one this modification increases its activity and for the other, it decreases it. When analyzing the *in vitro* results, at first sight, it could be thought that the amino group of **P2** is increasing toxicity as opposed to the hydroxyl group of **P1**, however, when **M1** and **M2** are compared, the opposite is observed.

Regarding **MC1** and **MC2** (Table 1, third and sixth lines), by linking cellulose nanocrystals to these metalla-assemblies, it was intended not only to increase the selectivity towards cancer cells (which cannot be tested *in vitro*, given that this selectivity is expected to come from the EPR effect) but also hydrophilicity, thus determining the effect on the PDT activity that this further modulation will bring. We can observe just by looking at the results that the IC_{50} decreases significantly when the metalla-assembly is grafted to CNCs. By analyzing the results, we can also determine that they follow the expected behavior, which is a lower IC_{50} when compared to their predecessors. This might be due to the improved solubility that is observed. From these results, it is possible to conclude that these new PDT agents, not only show enhanced chemical and structure stability but also increased hydrophilicity and consequently higher cytotoxicity.

It has been previously reported that one of the factors contributing to the greater efficiency of PDT is the accumulation of PS in tumor cells [49]. Therefore, this increase in the cytotoxicity of the more amphiphilic derivatives will, theoretically, be related to their increased uptake by

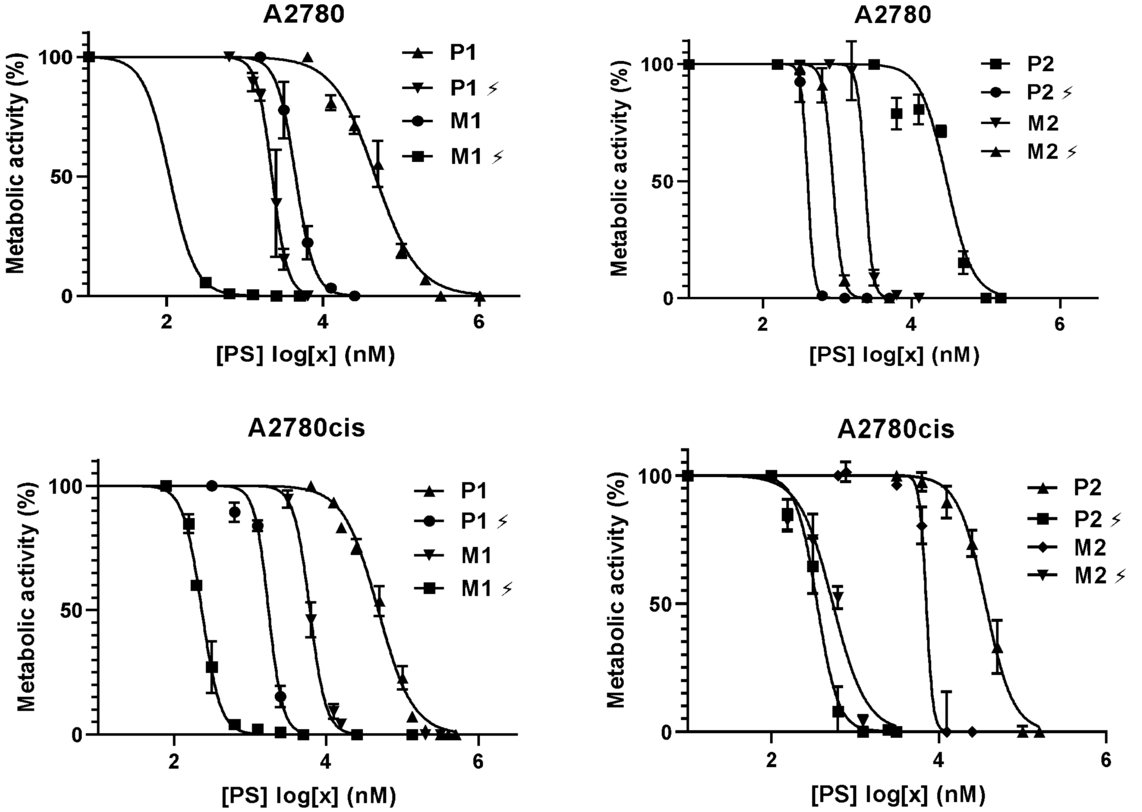

Fig. 6. Metabolic activity of **P1**, **P2**, **M1**, and **M2** against two different ovarian cancer cell lines (A2780 and A2780cis) with and without irradiation. Error bar stands for standard error (±SE), calculated from 3 repeated measurements.

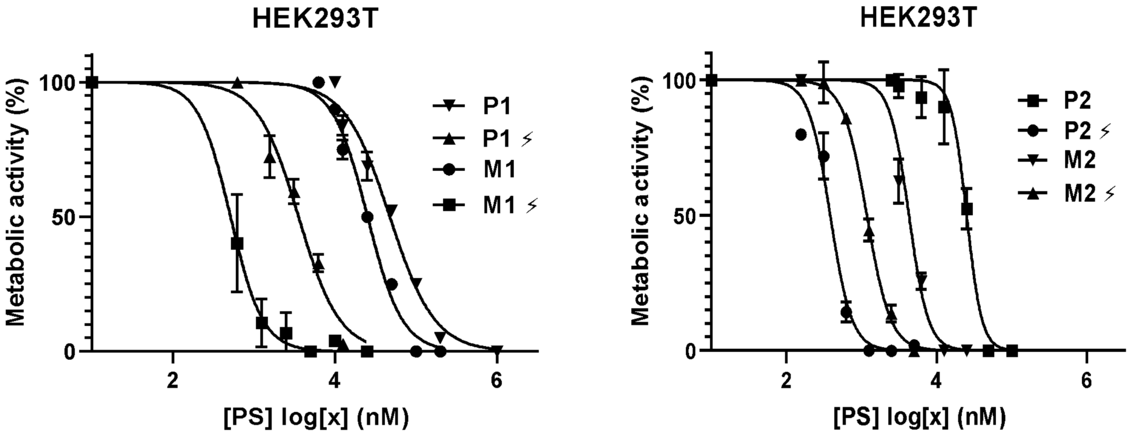

Fig. 7. Metabolic activity of **P1**, **P2**, **M1**, and **M2** against a normal liver cell line (HEK293T) with and without irradiation. Error bar stands for standard error (±SE), calculated from 3 repeated measurements.

cells. Furthermore, when the photodynamic activity of these compounds against the A2780 and A2780cis cell lines is compared, it can be concluded that there is no significant difference between the two. This is important because the A2780cis cell line is resistant to Cisplatin®, a standard metal-based chemotherapeutic drug to treat cancers, including ovarian cancer. Consequently, drugs that can inhibit its growth just as much as they would to normal A2780 cell lines are in need. These compounds seem to not discriminate between the two lines, especially when irradiation is applied, which is a very important and exciting result because they could potentially be used to treat cancers resistant to common oncogenic drugs such as Cisplatin®. Additionally, given that these compounds are built from arene ruthenium units, a classical *p*-cymene ruthenium PTA (PTA = 1,3,5-triaza-7-phosphaadamantane) chemotherapeutic RAPTA-C [50], was also tested and compared. When analyzed, the IC_{50} of RAPTA-C and of these metalla-assemblies show a significant difference: RAPTA-C has IC_{50} values always higher than

Copyright © 2023 World Scientific Publishing Company

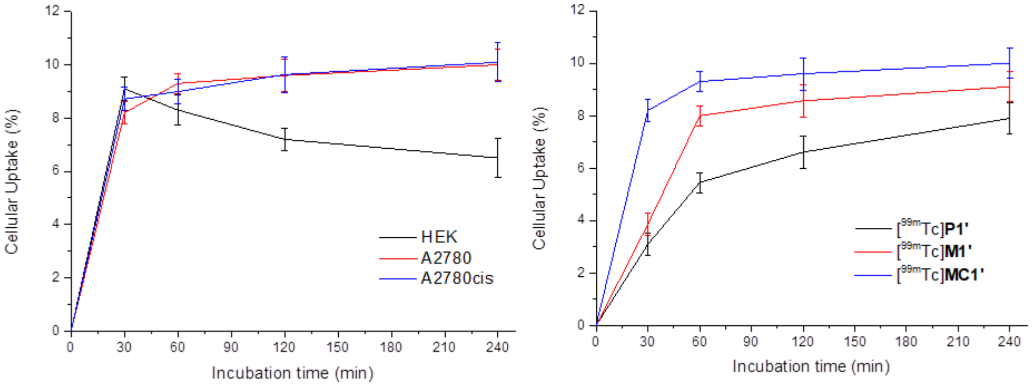

Fig. 8. Graph presenting the estimated cell uptake values expressed in % for [^{99m}Tc]**MC1′** in both A2780, A2780cis. and HEK293T cell lines (left); and graph presenting the estimated cell uptake values expressed in % for [^{99m}Tc]**P1′**, for [^{99m}Tc]**M1′**, and [^{99m}Tc]-**MC1′** in the A2780 cell line (right). Error bar stands for standard error (±SE), calculated from 3 repeated measurements.

200 µM, independently of the cell line, and no difference when irradiated, as expected since it doesn't have a photosensitive agent in its structure. Another interesting remark is that further functionalization of the initial porphyrins **P1** and **P2** are translated into not only lower IC$_{50}$ values when irradiation is applied, but also without irradiation, which means that the photodynamic efficiency is partially lost in the final **MC1** and **MC2** derivatives.

Finally, from all tested compounds, **M1** showed the best overall results *in vitro*, suggesting that **MC1** could work better *in vivo* when other factors such as the EPR effect can be considered as well. All the studied compounds revealed dose-dependent anti-proliferative effects. In addition, derivatives with increased hydrophilicity, obtained by cellulose linkage or by coordination with ruthenium metalla-clips, showed lower IC$_{50}$.

To evaluate their biodistribution, the ^{99m}Tc-labeled versions of these compounds were used in *in vivo* imaging animal models. An administered dose of 3 µg/ml was used, which is lower than the IC$_{50}$ without irradiation (> 8 µg/ml), but higher than the IC$_{50}$ with irradiation (< 1 µg/ml). Therefore, more imaging agents can be injected, without harming cells, since no radiation is used for this procedure. As expected by our previous metabolic activity assays, the internalization assay denoted a variation of cell uptake from 6 to 13% depending on cell lines. Indeed, a higher uptake in the A2780 cancer cells is observed over the normal liver cells HEK293T over time (Fig. 8). In addition, by increasing the size of the photosensitizer and upon grafting to CNCs, a faster and stronger uptake is observed (Fig. 8).

In vivo imaging studies

For the *in vivo* imaging studies, the radiolabelled compounds [^{99m}Tc]**M1′** and [^{99m}Tc]**MC1′** were selected, since they showed the most promising results *in vitro*, therefore showing the best characteristics for PDT and *in vivo* applications. Although [^{99m}Tc]**MC1′** was expected to be the ideal PS as a multimodal agent, due to the added CNC moiety which is supposed to help with targeting and distribution, [^{99m}Tc]**M1′** was also used in order to compare what this addition brings *in vivo*.

The protocol consisted of a 100 µL retro-orbital injection of either [^{99m}Tc]**M1′** or [^{99m}Tc]**MC1′** with radioactivity of approximately 100 µCi in SCID mice, with their consequent imaging at different time points. It should be noted that preliminary results using different concentrations of [^{99m}Tc]**MC1′**, more specifically 1500 nM and 750 nM were tested before achieving the ideal concentration of 375 nM. For this, an adequate volume for each desired concentration was taken so that in the final volume of 100 µL a 100 µCi radioactivity was conserved, each final solution was then topped with different amounts of water for injection to obtain a final volume of 100 µL so that the final concentrations were 375, 750 and 1500 nM respectively. This was possible because the radioactivity is not altered with the dilution of the solutions.

At the highest concentration (1500 nM), both compounds seemed to accumulate preferentially in the lungs instead of the liver and intestines (Fig. 9), which raised a question about animal welfare, and therefore the concentration was lowered to 750 nM. At this concentration, the excretion was similar to the one found later for 375 nM, but with some extra accumulation at the injection site (Fig. 10). This is thought to be the cause for the observed local photoreaction, which damaged the animal's eye (point of injection). Due to this, it was decided to lower the dose once again with the aim of trying to achieve the same imaging results with a lower concentration of compound to protect the animal while still giving good images of their biodistribution, and a concentration of 375 nM was selected. This concentration was considered safe through the analysis of the images for [^{99m}Tc]**MC1′**, which showed the expected accumulation at both the liver and the injection site for this compound, but with no evidence of photoreaction occurring (no damage to the eyes of the mice were observed as well as no mortality).

Through the analysis of the images acquired for [^{99m}Tc]-**M1′** (Fig. 11) and [^{99m}Tc]**MC1′** (Fig. 12) at 375 nM, it

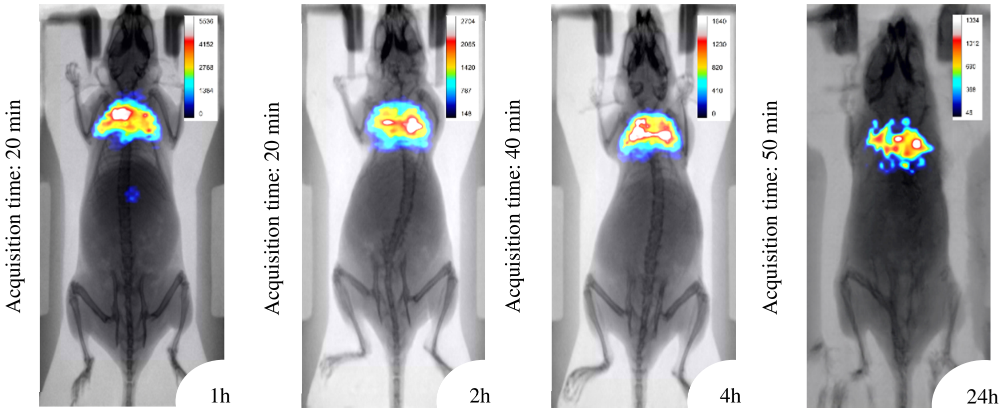

Fig. 9. Indicative static 20 – 50 min scintigraphy/X-ray images of a normal Swiss Albino mouse retro-orbital administered with [^{99m}Tc]**MC1′** (1500 nM) at 1, 2, 4 and 24 hours p.i. The gradual alteration in color indicates a lower to a higher number of recorded counts.

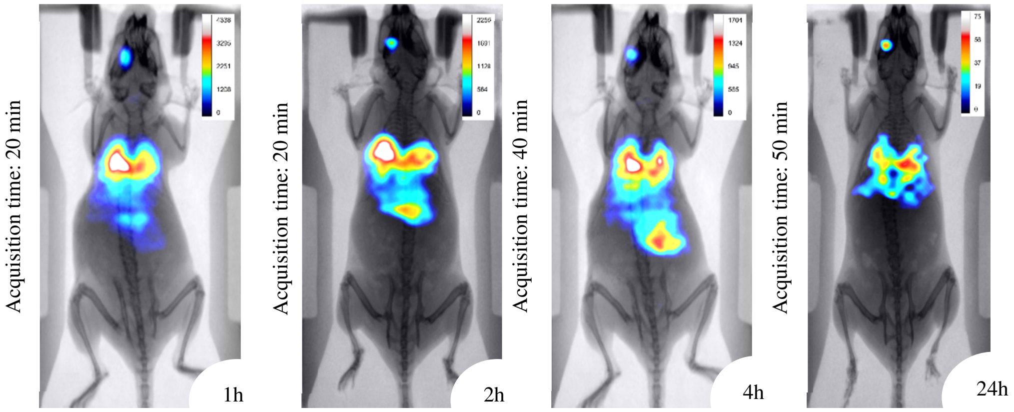

Fig. 10. Indicative static 20 – 50 min scintigraphy/X-ray images of a normal Swiss Albino mouse retro-orbital administered with [^{99m}Tc]**MC1′** (750 nM) at 1, 2, 4 and 24 hours p.i. The gradual alteration in colour indicates a lower to a higher number of recorded counts.

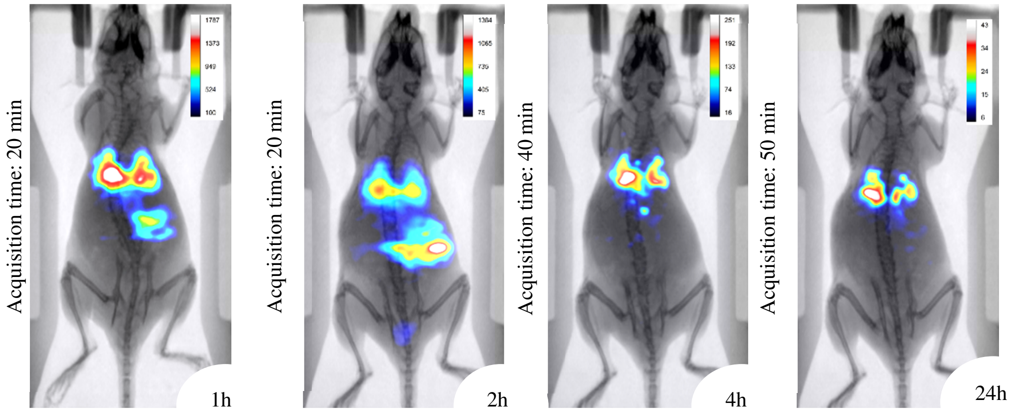

Fig. 11. Indicative static 20 – 50 min scintigraphy/X-ray images of a normal Swiss Albino mouse retro-orbital administered with [^{99m}Tc]**M1′** (375 nM) at 1, 2, 4 and 24 hours p.i. The gradual alteration in colour indicates a lower to a higher number of recorded counts.

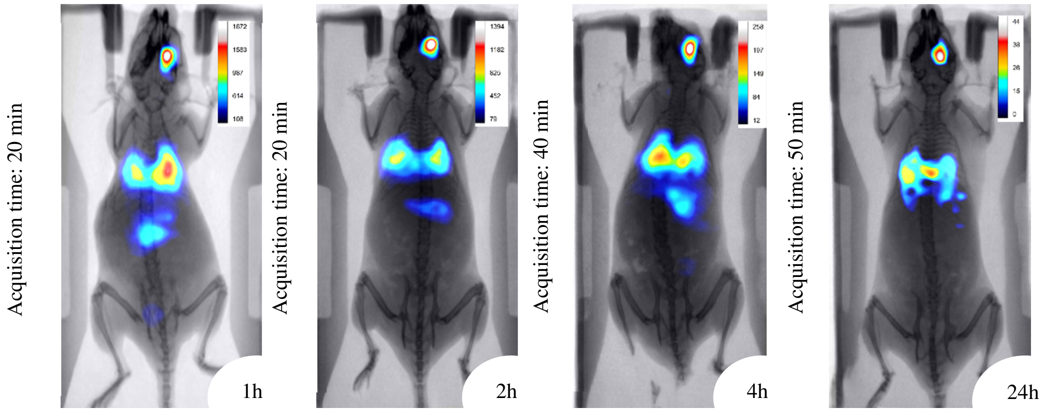

Fig. 12. Indicative static 20 – 50 min scintigraphy/X-ray images of a normal Swiss Albino mouse retro-orbital administered +with [^{99m}Tc]**MC1′** (375 nM) at 1, 2, 4 and 24 hours p.i. The gradual alteration in color indicates a lower to a higher number of recorded counts.

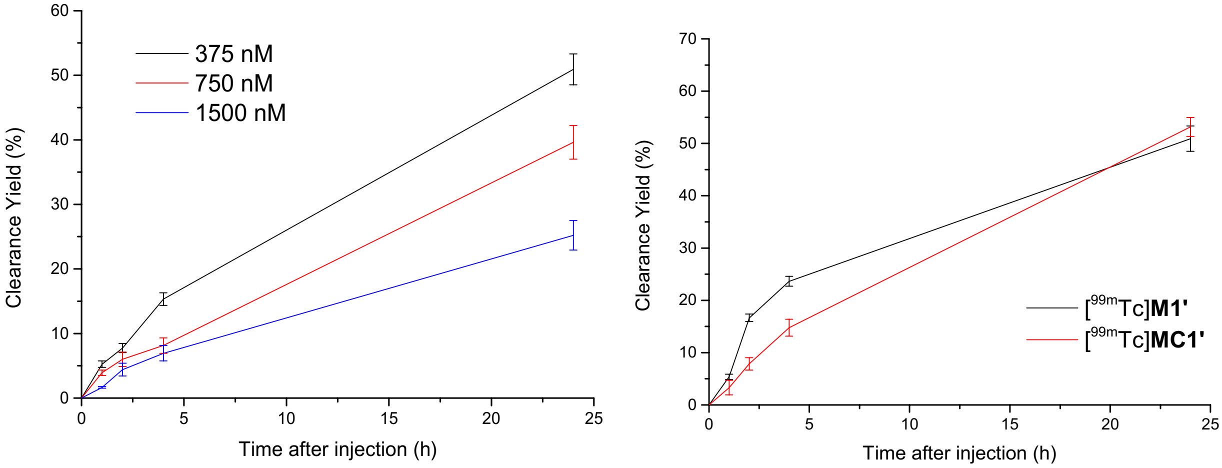

Fig. 13. Clearance yields for [^{99m}Tc]**MC1′** at different concentrations: 375, 750 and 1500 nM (left); and for [^{99m}Tc]**M1′**, and [^{99m}Tc]-**MC1′** at 375 nM (right). Error bar stands for standard error (±SE), calculated from three repeated measurements.

was clear that the circulation for both compounds from 1 to 24 h post-injection (p.i.) was very similar. Although with some accumulation in a portion of the intestines, in the first hour, they seem to accumulate preferentially in the liver. This is the most prominent, extending all the way to the 24 h mark, and it can suggest that these compounds if administered in a dose that has an effect without irradiation, could have some inherent hepatotoxicity. The accumulation or not of the compound at the injection site seems to be not related to size or concentration, given that at a lower concentration (375 nM) of [^{99m}Tc]**MC1′** higher accumulation is observed (Fig. 12) at the injection site as opposed to [^{99m}Tc]**MC1′** at a 750 nM concentration (Fig. 10). In fact, when a further look is taken into the clearance of the compounds (Fig. 13), similar clearances for all compounds suggest that the concentration of the injected solution rather is more relevant than if the compound is bound to the cellulose nanocrystals. This is better evidenced when we compare the 3 different concentrations of [^{99m}Tc]**MC1′** (375, 750, and 1500 nM) and notice that the higher the concentration administered, the longer it takes for the compound to be cleared. At 375 nM, for example, we have a clearance at 24 h of around 50%, while for 1500 nM, at the same time point, the clearance is less than half, being about 20%. Lastly, it seems that the grafting of CNC mostly exerts its influence at the clearance level at earlier time points and becomes less impactful the longer it stays in the body.

EXPERIMENTAL

Materials and analytical methods

All non-synthesized reagents were commercially available (Sigma-Aldrich, Brunschwig, Basel, Switzerland) and used as received. NMR spectra were recorded with a Bruker Advance Neo Ascend 600MHz spectrometer

(600.13 MHz for ^{1}H NMR spectra). UV–vis absorption spectra were recorded with a PerkinElmer UV−vis spectrophotometer (Waltham, MA, USA). Infrared spectra were recorded with a Thermo scientific Nicolet iS5 spectrometer. Electrospray ionization mass spectrometry (ESI-MS) was performed in positive or negative mode with an LCQ Finnigan mass spectrometer. Microanalyses were carried out by the Mikroelementaranalytisches Laboratorium, ETH Zürich (Zürich, Switzerland). Dynamic light scattering (DLS) was used for the measurement of average hydrodynamic diameters (Malvern Zetasizer Nano-ZS, Malvern Instruments, UK). Each suspension (0.025 wt%) in pure water was analyzed in triplicate at 20°C with a scattering angle of 173°. Pure water was used as a reference-dispersing medium. The ζ-potential data were collected through electrophoretic light scattering at 20°C, 150 V, in triplicate for each suspension (0.25 wt%) using the same instrument and at neutral pH. The instrument was calibrated with a Malvern -68 mV standard before each analysis cycle.

Technetium-99m in the form of $[^{99m}Tc]NaTcO_4$ was collected by elution of a $[^{99}Mo]Mo/[^{99m}Tc]Tc$ TEKCIS generator (Auckland, New Zealand) calibrated at 6 GBq, and all radiochromatography was performed with a miniGITA Dual radio TLC system by Elysia Raytest (Straubenhardt, Germany).

A2780 and A2780cis cell lines were obtained from the European Collection of Authenticated Cell Cultures (ECACC) and HEK293T cells were obtained from the American Type Culture Collection (ATCC, CRL-1619). All cell lines were maintained according to the suppliers' recommendations at 37°C in a humidified atmosphere with 95% air and 5% CO_2 in a HeraCell 150 incubator. Dulbecco's Modified Eagle's culture Medium (DMEM, Sigma D-5648) supplemented with 10% fetal bovine serum (Sigma F7524), 250 μM sodium pyruvate (Gibco 11360), and 1% antibiotic (100 U/ml penicillin and 10 μg/ml streptomycin; Sigma A5955) was used for the HEK293T cell line; while for the A2780 and A2780cis cell lines, Roswell Park Memorial Institute 1640 Medium (RPMI, Sigma R6504) culture medium supplemented with 10% fetal bovine serum, 1mM sodium pyruvate, and 1% antibiotic was used.

The *in vivo* studies were performed at the NCSR Demokritos (Aghia-Paraskevi, Attica Prefecture, Greece), using female SICD mice (15–25 g) purchased from the Breeding Facilities of the NCSR Demokritos (Permit Number: EL 25 BIO 019, EL 25 BIO 020). The protocol and all the animal procedures were approved by the General Directorate of Veterinary Services (Athens, Attica Prefecture, Greece) and by the Bioethical Committee of the Institution (Permit number: EL 25 BIO 022, EL 25 BIO 042) on the basis of the European Directive 2010/63/EU on the protection of animals used for experimental purposes. The imaging studies were performed on a dedicated benchtop mouse-sized gamma camera (γ-eye^{TM} by BioEmTech).

Synthesis

General procedure for the synthesis of the metallaclip C1, $[Ru_2(\eta^6\text{-}p\text{-cymene})_2\{2,5\text{-bis}(2\text{-hydroxyethylamino})\text{-}1,4\text{-benzoquinone}\}Cl_2]$

A mixture of 2,5-bis((2-hydroxyethyl)amino)-cyclohexa-2,5-diene-1,4-dione (52.0 mg, 0.23 mmol), CH_3COONa (38.4 mg, 0.46 mmol), and $[Ru(p\text{-cymene})Cl_2]_2$ (145.0 mg, 0.23 mmol), were dissolved in ethanol (25 mL) and stirred at reflux for 24 h. The reaction was allowed to cool to room temperature, the volume was reduced to half, and the mixture was stored in the refrigerator overnight. The precipitate was filtered off and washed with cold H_2O to isolate the desired product as a violet solid (71% yield).

^{1}H NMR (600 MHz, DMSO-d_6): δ (ppm) 7.30 (s, 2H, $CH_{ar\text{-}benzoquinone}$), 5.87 (d, 2H, $CH_{ar\text{-}cymene}$), 5.64 (d, 2H, $CH_{ar\text{-}cymene}$), 5.58 (d, 2H, $CH_{ar\text{-}cymene}$), 5.39 (d, 2H, $CH_{ar\text{-}cymene}$), 4.09 (s, 2H, OH), 3.76 (m, 4H, CH_2), 3.54 (m, 4H, CH_2), 2.51 (s, 6H, CH_3), 2.20 (br, 2H, $\mathbf{CH}(CH_3)_2$), 1.29 (m, 12H, $CH(C\mathbf{H}_3)_2$). **ESI-MS** (positive mode): $[C_{30}H_{42}Cl_2N_4O_2\text{-}Cl^-]^+$: Calcd 765.08 (m/z), Found 765.12 (m/z). **Elem anal.** Calcd for $C_{30}H_{42}Cl_2N_4O_2Ru_2$ (764.08): C, 47.18; H, 5.54; N, 7.34. Found: C, 47.21; H, 5.61; N, 7.37.

General procedure for the synthesis of metalla-assemblies M1 and M2

In a round bottom flask, 3 eq. of **C1** (37.5 mg) were suspended in MeOH (20 mL), and $AgCF_3SO_3$ (6 eq., 24 mg) was added. The mixture was stirred at RT for 3 h. At this point, **P1** (20 mg) or **P2** (20 mg) were added (2 eq.), and the mixture was heated to 60°C. The reaction was stirred for 24 h. Then, the solution was filtered to remove silver chloride and allowed to cool to room temperature. The solvent was removed under reduced pressure, and the crude product was dried overnight. CH_2Cl_2 (1 mL) was added to dissolve the solid, and diethyl ether was added to induce precipitation. The solid was filtered off and dried under vacuum (71% and 66% yield for **M1** and **M2**, respectively).

M1: **^{1}H-NMR:** (600 MHz, DMSO-d_6): δ (ppm) 8.78 (s, 16H, $CH_{ar\text{-}porphyrin}$), 8.29 (d, 12H, $CH_{ar\text{-}pyridine}$), 8.25 (d, 4H, $CH_{ar\text{-}phenyl}$), 8.21 (d, 12H, $CH_{ar\text{-}pyridine}$), 7.11 (d, 4H, $CH_{ar\text{-}phenyl}$), 5.82 (m, 12H, $CH_{ar\text{-}cymene}$), 5.71 (s, 6H, $CH_{ar\text{-}benzoquinone}$), 5.55 (d, 6H, $CH_{ar\text{-}cymene}$), 5.39 (d, 6H, $CH_{ar\text{-}cymene}$), 4.73 (s, 2H, OH_{phenol}), 4.10 (s, 6H, OH), 3.76 (m, 12H, CH_2), 3.53 (m, 12H, CH_2), 2.53 (s, 18H, CH_3), 2.20 (m, 6H, $\mathbf{CH}(CH_3)_2$), 1.29 (m, 36H, $CH(C\mathbf{H}_3)_2$), -2.90 (s, 4H, NH). **ESI-MS** (positive mode): [**M1**-$3CF_3SO_3$]$^{3+}$: Calcd 1267.2 m/z. Found 1267.2 m/z; [**M1**-$4CF_3SO_3$]$^{4+}$: Calcd 913.1 m/z. Found 913.1 m/z; [**M1**-$5CF_3SO_3$]$^{5+}$: Calcd 700.7 m/z. Found 700.7 m/z. **Elem anal.** Calcd for $C_{178}H_{174}F_{18}N_{20}O_{32}Ru_6S_6$ (4248.49): C, 50.35; H, 4.13; N, 6.60. Found: C, 51.01; H, 4.19; N, 6.67. **UV-vis** (C_2H_6OS): λ_{max}, nm (log ε) 412(5.59), 514(4.18), 550(3.74), 588(3.68), 649(3.52).

M2: **^{1}H-NMR:** (600 MHz, DMSO-d_6): δ (ppm) 9.05 (s, 16H, $CH_{ar\text{-}porphyrin}$), 8.87 (br, 12H, $CH_{ar\text{-}pyridine}$), 8.18 (d, 12H, $CH_{ar\text{-}pyridine}$, 7.61 (d, 4H, $CH_{ar\text{-}phenyl}$), 5.98 (br, 4H, NH_2), 5.81 (m, 12H, $CH_{ar\text{-}pyridine}$), 5.70 (s, 6H, $CH_{ar\text{-}benzoquinone}$) 5.39 (m, 12H, $CH_{ar\text{-}cymene}$), 4.12 (s, 6H, OH), 3.76 (m, 12H, CH_2), 3.52 (m, 12H, CH_2), 2.55 (s, 18H, CH_3), 2.20 (m, 6H, C**H**(CH_3)$_2$), 1.30 (m, 36H, CH(C**H**$_3$)$_2$), -2.90 (s, 4H, NH). **ESI-MS** (positive mode): [**M2**-3CF_3SO_3]$^{3+}$: Calcd 1266.5 m/z. Found: 1266.5 m/z; [**M2**-4CF_3SO_3]$^{4+}$: Calcd 912.6 m/z. Found: 912.6 m/z; [**M2**-5CF_3SO_3]$^{5+}$: Calcd 700.3 m/z. Found: 700.3 m/z. **Elem anal.** Calcd for $C_{178}H_{176}F_{18}N_{22}O_{30}Ru_6S_6$ (4246.52): C, 50.37 H, 4.18; N, 7.26. Found: C, 50.41; H, 4.41; N, 7.60. **UV-vis** (C_2H_6OS): λ_{max}, nm (log ε) 415(5.72), 513(4.23), 549(3.86), 587(3.78), 648(3.57).

General procedure for the synthesis of metalla-assemblies linked to CNCS MC1 and MC2

First, CNCs were prepared and characterized according to the literature [17, 51]. Then, the oxidation of the primary hydroxyl groups of the cellulose nanocrystals to COOH functions was performed, also following a well-established protocol [16]. For the grafting of **M1** and **M2,** two 50 ml solutions of oxidized CNCs (1 eq.) in deionized water were activated with NHS (2 eq.) and ethylene dichloride (2 eq.) each for 2 h at room temperature. Each metalla-assembly (**M1** or **M2**; 1 eq.) was then dissolved in 20 mL of methanol and added dropwise to the respective oxidized CNCs solution. The mixture was left to react for 24 h. After stirring for 1 day at room temperature, the CNC-metalla-assemblies (**MC1** and **MC2**) were recovered by ultracentrifugation at 13000 rpm, after several washes with deionized water. The final solutions were collected and both z-average size and also zeta potential were determined. For compound **MC1**, for example, these values were 184.2 nm (Fig. S9, supplementary information), and -38.3 ± 4.5 mV (Fig. S10, supplementary information), respectively.

Radiochemistry

[^{99m}Tc]Pertechnetate was first eluted from a [^{99}Mo] Mo/[^{99m}Tc]Tc generator. After elution, a 74 MBq aliquot was then reduced with 0.5 ml of a solution of 0.1 mg $SnCl_2$ in 0.05 N HCl. After shaking vigorously for 1 min and allowing to stand at room temperature for 15 min, the pH of the reduced technetium-99m solution was adjusted to 7.4 with a NaOH 1M solution. A 1 mL aliquot of **P1**, **M1** or **MC1**, previously dissolved in DMSO and diluted to a concentration of 10 mg/ml, was then added to the neutralized [^{99m}Tc]Tc$SnCl_2$ mixture and incubated at 45°C for 30–60 min depending on the porphyrin/metalla-cage, and consequently labeled with ~55.5 MBq of technetium-99m by the chemical method described above. The incorporation efficiency is assessed by ascending paper radiochromatography with Whatman 1 MM paper developed in acetone or saline as the mobile phase. The radiolabeling was successful with all compounds achieving radiochemical incorporation higher than 93%.

For the radiochemical purity studies performed with the radiolabeled compounds, in order to follow their stability, various media were tested including saline, phosphate-buffered saline (PBS), deionized water, HEPES (2-[4-(2-hydroxyethyl)piperazin-1-yl]ethanesulfonic acid) buffer solution (0.5 M, pH 5–6), ammonium acetate (0.5 M, pH 5.5), Plasma-Lyte 148 (pH 7.4), and saturated EDTA and DTPA solutions, at different time points (15, 30, 60, 120, 240 min, and 24 h). The stability was investigated by incubating the radiolabeled compound in the media (1:10) and was then evaluated through ascending paper radiochromatography with Whatman 3MM paper developed in saline for all ^{99m}Tc-labeled compounds. From this, it was possible to conclude when the reaction was completed, because the radio-TLC peak for the labeled compounds can be seen at the front of the radio-TLC, while if it is incomplete, traces of reduced technetium-99m stay at the origin.

In vitro

The cytotoxicity and therapeutic efficacy of the compounds as photosensitizers were assessed after their synthesis and characterization. A metabolic activity assay was used to determine their activity. Because the goal of this study was to synthesize and characterize porphyrin metalla-assemblies grafted to cellulose nanocrystals, as well as to assess their potential as a photosensitizer agent in cancer PDT, the choice of carcinogenic cell lines was critical. Three human cell lines were used: the A2780 human ovarian cancer cell line and the cisplatin-resistant cell line A2780 cis, as well as the HEK293T cell line, originally derived from human embryonic kidney cells, that we used as an additional control to assess tumor specificity.

Metabolic activity

The cytotoxicity of the photosensitizers in all cell lines was tested using an MTT (3-(4,5-dimethylthiazol-2-yl)-2,5-diphenyltetrazolium bromide) colorimetric assay to establish their potential therapeutic impact and to examine the sensitivity of the cell lines to the compounds. 96-Well plates of the A2780, A2780cis, and HEK293T cell lines were prepared for this experiment. Cell culture media was aspirated, and the plates were cleaned with PBS 48 hours after being subjected to the methods outlined in the preceding section. After that, each well was filled with 100 mL of MTT (0.5 mg/ml; Sigma M2128) in PBS, pH 7.4, and each plate was incubated in the dark at 37°C for at least 3 hours. The contents of each well were homogenized after all formazan crystals have been produced and solubilized with DMSO. Using the Molecular Devices® SpectraMax M5E multi-mode plate reader, the absorbance was measured at 570 nm with a 620 nm reference filter.

The obtained results were evaluated and processed using the OriginPro 9.0 program and were expressed as a percentage of metabolically treated cells against non-treated cells. For each compound, dose-response curves were constructed, and IC_{50} (half-maximal inhibitory concentration) values were calculated. Dark cytotoxicity tests were carried out as described previously, but without the irradiation phase and with larger sensitizer concentrations (5 to 20 mM). This approach allowed for the creation of dose-response curves and the determination of the sensitizer concentration that suppresses the metabolic activity of the cultures by 50%

Internalization assays

Cells were seeded in a 12-well plate (~10^5 cells/well) overnight at 37°C in a humidified incubator containing 5% CO_2. To the vial with the radiolabeled compound, the cell culture medium was added until the 2ml mark, giving a final concentration of 50 μg/ml of the compound with 37 to 55.5 MBq. Then, it was added 5.5–7.5 MBq of this solution to each well (A2780, A2780cis, or HEK293T cell lines), which was previously washed with phosphate-buffered saline (PBS) in order to remove any non-attached or dead cells.

The amount of activity added was measured in a dose-calibrator. This process was repeated for the different wells in the 12 well plates, and after they were left to incubate for different time periods varying from 15 minutes to 4 h. At the end of the desired time point, the wells were washed for at least 3 times with PBS. This step assures that any radioactivity that doesn't enter the cells or attach to their membrane is removed, so the results are accurate and truly represent the uptake process. These washes were collected, and their activity was measured. After washing, cold methanol was used 2 or 3 times to lyse the cells and collect any compound that was inside them. Finally, the resulting lysate in each well was collected and the activity was measured again in a dose-calibrator as previously described. Each condition was currently being performed in triplicates and the experiments were repeated three times as well in order to assure the results were reliable and reproducible.

Photodynamic treatment

Cells were plated and incubated in the incubator overnight for each experiment to allow for cell attachment. Mother solutions at 20 mM in DMSO (Fisher Chemical, 200-664-3) of each photosensitizer were made and diluted to the necessary quantities (from 10 nM to 10 mM). Untreated cell cultures were included as controls on each plate. The light-treated cell cultures were always incubated for 48 h at the optimal photosensitizer doses. The cultures were irradiated for 30 minutes with an irradiance of 10 mW/cm^2, (18 J/cm^2 light dose) with the setup described in detail by Joniova *et al*. [52]. Irradiations at a wavelength of 652 nm were performed with a diode laser (Ceralas D-50, BIOLITEC, Germany) coupled to a frontal light distributor (FD-1, Medlight SA, Switzerland) for photodynamic therapy.

In vivo imaging protocol

Following radiolabeling, the resulting solution was diluted with water to a concentration of 375 nM, with a final volume of 80–100 μL and a final activity of 3.3–3.7 MBq (90–110 μCi): the activity being calculated by measuring in a dose calibrator the syringe before and after the administration. After being previously anesthetized with isoflurane (3.5% for induction), a SCID mouse was injected retro-orbitally, and a scintigraphic imaging profile in normal SCID mice was acquired. The mice were positioned on the animal bed at a <0.5 cm distance from the camera head to allow whole-body imaging with maximum spatial resolution and successive 2 min frames were collected for up to 1 h post-injection (p.i.). After the first hour, static images were also acquired at 1, 2, 4, and 24 h p.i.

The activity in the animal was also measured for each time point to determine the clearance yield of the compound through the difference of the expected activity if none of it was cleared out of the body, with the activity being corrected for the expected decay at each time-point, and the actual activity measured in the mouse. The animal was left to regain consciousness between time points in order to let the natural biodistribution of the compound occur without any external factors. At each time point, one mouse was anesthetized with isoflurane (3.5% for induction), placed on the animal bed of the stepping apparatus, and maintained under anesthesia (2% for maintenance) and at 37°C by the air flow heated bed throughout the imaging procedure.

Under each condition, a set of 3 SCID mice was used. Acquisition times varied from 20 to 60 min depending on the timepoint and radioactivity decay in the animal, meaning that for lower activities, a longer acquisition time was needed to acquire a better image. The data acquired was treated with the help of ImageJ® software to reconstruct the images.

CONCLUSIONS

This study showed very promising results regarding the synthesis and functionalization of multimodal agents for PDT treatment. The combination of cellulose nanocrystals with porphyrin-based metalla-assemblies was intended to ameliorate their delivery, solubility, and metabolism activity, while still keeping the photo-activity of the compounds. Indeed, the synthesized and characterized stable metalla-assemblies grafted to cellulose nanocrystals have demonstrated photochemical properties suitable for PDT and imaging applications.

In addition, they show no tendency to aggregate, possibly because of the steric and electrostatic nature of the

CNCs and metalla-assemblies. Secondly, the radiolabeling of these compounds has been successful, and although some adjustments to the protocol might be needed for cellular uptake assays, preliminary experiments show promising results and potential for these molecules to be used not only as therapeutic but also as diagnostic agents. Finally, the *in vitro* photodynamic effect of these photosensitizers has shown to be promising for therapeutic applications having IC_{50} values in the nanomolar range in ovarian cancer cells, and preferential cellular uptake from cancer cells in comparison to normal liver cells.

In the future, we would like to explore other relevant characteristics for their possible use as imaging agents in PDT, by the conjugation of such compounds with chelator agents and the introduction of other radionuclides with different half-times for SPECT *in vivo* imaging. In addition, we would like to complete the photophysical studies (calculate quantum yields of fluorescence, triplet state formation, and singlet oxygen production), to gain further insights into their photochemical properties.

Acknowledgments

This project has received financial support from the European Union's Horizon 2020 research and innovation program under the Marie Skłodowska-Curie grant agreement n°764837.

Supporting information

^{1}H-NMR (Figs. S1 and S2), mass spectrometry analysis (Figs. S3 and S4), UV-Vis (Figs. S5–S7), and FTIR spectra (Fig. S8), as well as the z-average size and zeta potential (Figs. S9 and S10) are given in the supplementary material. This material is available free of charge *via* the Internet at https://www.worldscientific.com/doi/suppl/10.1142S1088424623500499

REFERENCES

1. McGuire S. *Adv. Nutr.* 2016; **7**: 418–419.
2. Simões JCS, Sarpaki S, Papadimitroulas P, Therrien B and Loudos G. *J. Med. Chem.* 2020; **63**: 14119–14150
3. Ethirajan M, Chen Y, Joshi P and Pandey RK. *Chem. Soc. Rev.* 2011; **40**: 340–362.
4. Bechet D, Couleaud P, Frochot C, Viriot ML, Guillemin F and Barberi-Heyob M. *Trends Biotechnol.* 2008; **26**: 612–621.
5. Emerich DF and Thanos CG. *J. Drug Target.* 2007; **15**: 163–183.
6. Konan YN, Gurny R and Allémann E. *J. Photochem. Photobiol. B Biol.* 2002; **66**: 89–106.
7. Heinrich A-K, Lucas H, Schindler L, Chytil P, Etrych T and Mueller T. *Mol. Cancer Ther.* 2016; **15**: 998–1007.
8. Tsai HC, Tsai CH, Lin SY, Jhang CR, Chiang YS and Hsiue GH. *Biomaterials* 2012; **33**: 1827–1837.
9. Kobayashi H, Watanabe R and Choyke PL. *Theranostics* 2013; **4**: 81–89.
10. Vonarbourg A, Passirani C, Saulnier P and Benoit JP. *Biomaterials* 2006; **27**: 4356–4373.
11. Jokerst J V., Lobovkina T, Zare RN and Gambhir SS. *Nanomedicine* 2011; **6**: 715–728.
12. Akhlaghi SP, Peng B, Yao Z and Tam KC. *Soft Matter.* 2013; **9**: 7905–7918.
13. Samir MASA, Alloin F and Dufresne A. *Biomacromolecules* 2005; **6**: 612–626.
14. Roman M. *Ind. Biotechnol.* 2015; **11**: 25–33.
15. Thompson L, Azadmanjiri J, Nikzad M, Sbarski I, Wang J and Yu A. *Rev. Adv. Mater. Sci.* 2019; **58**: 1–16.
16. Chauhan P, Hadad C, Sartorelli A, Zarattini M, Herreros-López A, Mba M, Prato M, Prato M and Carofiglio T. *Chem. Commun.* 2013; **49**: 8525–8527.
17. Drogat N, Granet R, Le Morvan C, Bégaud-Grimaud G, Krausz P and Sol V. *Bioorg. Med. Chem. Lett.* 2012; **22**: 3648–3652.
18. Le Guern F, Ouk TS, Grenier K, Joly N, Lequart V and Sol V. *J. Mater. Chem. B* 2017; **5**: 6953–6962.
19. Anaya-Plaza E, van de Winckel E, Mikkilä J, Malho JM, Ikkala O, Gulías O, Bresolí-Obach R, Agut M, Nonell S, Torres T, Kostiainen MA and de la Escosura A. *Chem. Eur. J.* 2017; **23**: 4320–4326.
20. Feese E, Sadeghifar H, Gracz HS, Argyropoulos DS and Ghiladi RA. *Biomacromolecules* 2011; **12**: 3528–3539.
21. Imlimthan S, Otaru S, Keinänen O, Correia A, Lintinen K, Santos HA, Airaksinen AJ, Kostiainen MA and Sarparanta M. *Biomacromolecules* 2019; **20**: 674–683.
22. Kano K, Minamizono H, Kitae T and Negi S. *J. Phys. Chem.* 1997; **101**: 6118–6124.
23. Sun Y and Stang PJ. *Aggregate* June 2021: e94.
24. Mari C, Pierroz V, Ferrari S and Gasser G. *Chem. Sci.* 2015; **6**: 2660–2686.
25. Pobłocki K, Drzeżdżon J, Kostrzewa T and Jacewicz D. *Int. J. Mol. Sci.* 2021; **22**: 8052.
26. Yu G, Yu S, Saha ML, Zhou J, Cook TR, Yung BC, Chen J, Mao Z, Zhang F, Zhou Z, Liu Y, Shao L, Wang S. Gao C, Huang F, Stang PJ and Chen X, *Nat. Commun*. 2018; **9**: 4335.
27. Barry NPE, Karim NHA, Vilar R and Therrien B, *Dalton Trans.* 2009; **48**: 10717–10719.
28. Schmitt F, Barry NPE, Juillerat-Jeanneret L and Therrien B. *Bioorg. Med. Chem. Lett.* 2012; **22**: 178–180.
29. Schmitt F, Barry NPE, Juillerat-Jeanneret L, Süss-Fink G and Therrien B. *J. Am. Chem. Soc.* 2012; **134**: 754–757.
30. Therrien B. *Chem. - Eur. J.* 2013; **19**: 8378–8386.
31. Gallardo-Villagrán M, Paulus L, Champavier Y, Leger DY, Therrien B and Liagre B. *J. Porphyr. Phthalocyanines* 2022; **26**: 533–541.

32. Therrien B and Furrer J. *Adv. Chem.* 2014; **2014**: 1–20.
33. Makhseed S, Machacek M, Alfadly W, Tuhl A, Vinodh M, Simunek T, Novakova V, Kubat P, Rudolf E and Zimcik P. *ChemComm.* 2013; **49**: 11149–11151.
34. Bogaards A, Sterenborg HJCM, Trachtenberg J, Wilson BC and Lilge L. *Lasers Surg. Med.* 2007; **39**: 605–613.
35. Stefflova K, Chen J and Zheng G. *Front. Biosci.* 2007; **12**: 4709–4721.
36. Waghorn PA. *J. Label. Compd. Radiopharm.* 2014; **57**: 304–309.
37. Subbarayan M, Shetty SJ, Srivastava TS, Noronha OPD and Samuel AM. *J. Porphyr. Phthalocyanines* 2001; **5**: 824–828.
38. Liu J, Yang Y, Zhu W, Yi X, Dong Z, Xu X, Chen M, Yang K, Lu G, Jiang L and Liu Z. *Biomaterials* 2016; **97**: 1–9.
39. Aguilar-Ortíz E, Jalilian AR and Ávila-Rodríguez MA. *Medchemcomm* 2018; **9**: 1577–1588.
40. Ciaffaglione V, Waghorn PA, Exner RM, Cortezon-Tamarit F, Godfrey SP, Sarpaki S, Quilter H, Dondi R, Ge H, Kociok-Kohn G, Botchway SW, Eggleston IM, Dilworth JR and Pascu SI. *Bioconjug. Chem.* 2021; **32**: 1374–1392.
41. Murugesan S, Shetty SJ, Srivastava TS, Noronha OPD and Samuel AM. *Appl. Radiat. Isot.* 2001; **55**: 641–646.
42. Bedel-Cloutour CH, Mauclaire L, Saux A and Pereyre M. *Bioconjug. Chem.* 1996; **7**: 617–627.
43. Barry NPE, Zava O, Furrer J, Dyson PJ and Therrien B. *Dalt. Trans.* 2010; **39**: 5272–5277.
44. Le Guern F, Ouk TS, Yerzhan I, Nurlykyz Y, Arnoux P, Frochot C, Leroy-Lhez S and Sol V. *Molecules.* 2021; **26**: 1122.
45. Ding L, Casas C, Etemad-Moghadam G, Meunier B and Cros S, *New J. Chem.* 1990, **14**: 421–431
46. Govindaswamy P, Süss-Fink G, Wee HA, Dyson PJ, Juillerat-Jeanneret L and Therrien B. *J. Med. Chem.* 2008; **51**: 1811–1816.
47. Hospodarova V, Singovszka E and Stevulova N. *Am. J. Anal. Chem.* 2018; **9**: 303–310.
48. Hemraz UD, Campbell KA, Burdick JS, Ckless K, Boluk Y and Sunasee R. *Biomacromolecules* 2015; **16**: 319–325.
49. Abrahamse H and Hamblin MR. *Biochem. J.* 2016; **473**: 347–364.
50. Weiss A, Berndsen RH, Dubois M, Müller C, Schibli R, Griffioen AW, Dyson PJ and Nowak-Sliwinska P. *Chem. Sci.* 2014; **12**: 4742–4748.
51. Ndong Ntoutoume GMA, Granet R, Mbakidi JP, Brégier F, Léger DY, Fidanzi-Dugas C, Lequart V, Joly N, Liagre B, Chaleix V and Sol V. *Bioorganic Med. Chem. Lett.* 2016; **26**: 941–945.
52. Joniova J, Kazemiraad C, Gerelli E and Wagnières G. *J. Photochem. & Photobiol., B: Biol.*, 2021; **225**: 112347.
53. Kamelnia E, Divsalar A, Darroudi M, Yaghmaei P and Sadri K. *Intl. J. Biol. Macromol.*, 2020; **146**: 299–310.